

Core-shell structured γ -Fe₂O₃@SiO₂@AgBr:Ag composite with high magnetic separation efficiency and excellent visible light activity for acid orange 7 degradation

Baozhu Tian*, Tingting Wang, Rongfang Dong, Shenyuan Bao, Fan Yang, Jinlong Zhang*

Key Lab for Advanced Materials and Institute of Fine Chemicals, East China University of Science and Technology, 130 Meilong Road, Shanghai 200237, PR China

ARTICLE INFO

Article history:

Received 27 May 2013

Received in revised form 9 August 2013

Accepted 15 August 2013

Available online 28 August 2013

Keywords:

Core-shell structure

Photocatalytic degradation

AgBr

Magnetic separation

Acid orange 7

ABSTRACT

Core-shell structured γ -Fe₂O₃@SiO₂@AgBr:Ag composite microspheres with narrow size distribution were synthesized by a versatile multistep route, including solvothermal method to fabricate magnetic core, modified Stöber method to coat SiO₂ interlayer, electrostatic assembly to deposit AgBr shell, and light reduction to form Ag nanoparticles. Spherical core with a diameter of 250 nm consists of primary magnetic nanoparticles, making the composite photocatalyst show high saturation magnetization under the premise of keeping a certain superparamagnetic property. SiO₂ interlayer with a thickness of ~15 nm is uniformly coated on the surface of magnetic core, favorable to enhancing the chemical stability of magnetic core as well as preventing the deterioration of photocatalytic activity. γ -Fe₂O₃@SiO₂@AgBr:Ag composite exhibits excellent visible light photocatalytic activity for the degradation of acid orange (AO7) dye, due to the fact that both Ag nanoparticles and AgBr can respond to visible light. Beneficial from the narrow size distribution as well as high saturation magnetization and superparamagnetic property, the core-shell structured photocatalyst shows high efficiency in magnetic separation and recovery. The optimal loading amount of AgBr for obtaining both uniform morphology and high activity is ~42 wt.%.

© 2013 Elsevier B.V. All rights reserved.

1. Introduction

Over the past few decades, semiconductor photocatalysis has attracted considerable attention as an environmentally friendly technology to remove harmful organic pollutants in waste water [1]. Among various semiconductor materials, TiO₂ has been widely studied because of its excellent optical and electronic properties, low cost, and photochemical stability [2,3]. However, pristine TiO₂ can only be excited by UV light because of its wide band gap, which leads to low utilization efficiency of the solar spectrum. To meet the requirement of future environmental technologies driven by solar energy, considerable efforts have been devoted to the exploitation of new and more efficient visible light-active photocatalysts. The strategies used for fabricating visible light-active photocatalysts can be classified into two categories: the first involves metal/nonmetal doping [4–7] or anchoring organic sensitizers [8,9] for wide-band-gap semiconductors; the second is to exploit new narrow-band-gap semiconductors such as CdS [10], BiWO₆ [11], and Ni_xTaO₄ ($x = 0\text{--}0.2$) [12]. Unfortunately, these

photocatalysts are still incompetent for practical applications because of a limited visible light response and low stability [9–13].

Noble metal nanoparticles (NPs), such as Au, Ag, Pt, and Cu, can strongly absorb visible light because of their surface plasmon resonance (SPR) [14]. Therefore, noble metal NPs can serve as an alternative type of sensitizers to enhance the visible light absorption of photocatalysts without the problem of degradation encountered with organic sensitizers [15,16]. In 2008, Huang et al. [17] fabricated visible light-active Ag@AgCl plasmonic photocatalyst by an ion-exchange method, which exhibited excellent photocatalytic activity under visible light irradiation. From then on, researchers began to pay attention to AgX (X=Cl, Br, and I)-based plasmonic photocatalysts [18,19]. Up to now, this kind of materials has been successfully applied in the degradations of non-biodegradable dyes, alcohols, and phenols in waste water [18,19].

For nano- or micro-sized photocatalysts, another problem that restrains their application in waste water treatment is how to effectively separate the used photocatalysts [20,21]. Centrifugation and filtration always lead to serious catalyst loss as well as high energy consumption [22], while traditional catalyst immobilization usually decreases the effective surface area [21]. In contrast, immobilizing catalysts on the surface of magnetic nano- or microparticles is an effective way to solve the above problem, by which the catalysts can be easily separated by an external

* Corresponding authors. Tel.: +86 21 64252062; fax: +86 21 64252062.

E-mail addresses: baozhutian@ecust.edu.cn (B. Tian), jinlongzhang@ecust.edu.cn (J. Zhang).

magnet under the premise of keeping photocatalytic activity [23]. Recently, $\text{Fe}_3\text{O}_4@\text{SiO}_2@\text{AgX}$ ($\text{X}=\text{Cl}$, Br , or I) photocatalysts have been prepared by immobilizing AgX on silica-coated magnetic Fe_3O_4 particles [24–26]. These composite photocatalysts can be successfully separated by applying an external magnetic field. However, there are still some deficiencies, such as wide size distribution [24], irregular morphological structures [25], and low AgX loading amount [26], which are harmful to separation efficiency and photocatalytic activity. For instance, An et al. [25] reported that the majority of $\text{Fe}_3\text{O}_4@\text{SiO}_2@\text{AgCl}$ nanoparticles can be magnetically separated within 1 min, but as long as 30 min is needed to completely harvest the nanoparticles. This phenomenon is probably due to the fact that the bigger particles can rapidly respond to the external magnetic field while the smaller ones cannot. To attain both high separation efficiency and photocatalytic activity, it is necessary of exploring an effective route to fabricate core–shell structured $\text{Fe}_3\text{O}_4@\text{SiO}_2@\text{AgX}$ composite with narrow size distribution as well as high AgX loading amount.

Herein, we fabricated core–shell structured $\gamma\text{-Fe}_2\text{O}_3@\text{SiO}_2@\text{AgBr:Ag}$ composite microspheres with narrow size distribution by a versatile multistep route, including solvothermal method to fabricate magnetic core, modified Stöber method to coat SiO_2 interlayer, electrostatic assembly to deposit AgBr shell, and light reduction to form Ag nanoparticles. The constructed composite improves separation efficiency and photocatalytic activity by following mechanisms: spherical magnetic core consists of many $\gamma\text{-Fe}_2\text{O}_3$ primary nanoparticles, making the composite microspheres show high saturation magnetization under the premise of keeping a certain superparamagnetic property, which is favorable to rapid magnetic separation and recovery; SiO_2 interlayer not only enhances the chemical stability of $\gamma\text{-Fe}_2\text{O}_3$ core but also restrains the deterioration of photocatalytic activity; the cooperation of AgBr and Ag nanoparticles makes the composite photocatalyst can effectively harvest visible light, which is favorable to the improvement of photocatalytic activity. The structural, magnetic, and optical performances of the core–shell structured $\gamma\text{-Fe}_2\text{O}_3@\text{SiO}_2@\text{AgBr:Ag}$ photocatalyst were characterized by scanning electron microscopy (SEM), transmission electron microscopy (TEM), X-ray diffraction (XRD), X-ray photoelectron spectroscopy (XPS), vibrating sample magnetometer (VSM), and UV-vis diffuse reflectance spectra (UV-vis DRS). The photocatalytic activity of $\gamma\text{-Fe}_2\text{O}_3@\text{SiO}_2@\text{AgBr:Ag}$ composite was evaluated in terms of the degradation of acid orange 7 (AO7) under visible light ($\lambda > 420 \text{ nm}$) irradiation, while the magnetic separation and recover tests were carried out by using a cubic Nd-Fe-B magnet.

2. Experimental

2.1. Materials

Ferric chloride hexahydrate ($\text{FeCl}_3 \cdot 6\text{H}_2\text{O}$), polyethylene glycol-20000 (PEG-20000), ethanol ($\text{C}_2\text{H}_5\text{OH}$), ethylene glycol (EG), sodium acetate (CH_3COONa), tetraethyl orthosilicate (TEOS, 28 wt.%), potassium bromide (KBr), and ammonium hydroxide (25 wt.% $\text{NH}_3 \cdot \text{H}_2\text{O}$) were purchased from Sinopharm Chemical Reagent Co. Ltd., China. Silver nitrate (AgNO_3) was obtained from Shanghai Chemical Reagent Co. Ltd. All of the chemicals were analytical grade and used without further purification.

2.2. Fabrication of photocatalyst

2.2.1. Magnetic Fe_3O_4

Magnetic Fe_3O_4 submicrospheres were synthesized by solvothermal method. Under magnetic stirring, 1.69 g of $\text{FeCl}_3 \cdot 6\text{H}_2\text{O}$ and 4.5 g of CH_3COONa were added into 50 mL of

EG solution containing 1.24 g of PEG-20000. After being stirred at 50 °C for 30 min, the mixture was transferred into a teflon-inner-liner stainless autoclave and kept at 180 °C for 10 h. Finally, the resulting precipitate (Fe_3O_4) was separated from the mother liquor by centrifugation, washed thoroughly with ethanol and double deionized water (DD-water), and dispersed in 50 mL of ethanol solution.

2.2.2. Core–shell structured $\text{Fe}_3\text{O}_4@\text{SiO}_2$

Core–shell structured $\text{Fe}_3\text{O}_4@\text{SiO}_2$ was fabricated by a modified Stöber method. Typically, 10 mL of the above ethanol solution containing Fe_3O_4 was mixed with 80 mL of ethanol and 10 mL of DD-water, followed by adding 0.10 mL of TEOS. After the suspension was sonicated for 30 min, 1 mL of $\text{NH}_3 \cdot \text{H}_2\text{O}$ was added dropwise and further reacted for 6 h. Finally, the product was washed with ethanol and DD-water several times.

2.2.3. Magnetic $\gamma\text{-Fe}_2\text{O}_3@\text{SiO}_2@\text{AgBr:Ag}$

$\text{Ag}(\text{NH}_3)_2^+$ solution was beforehand prepared by dissolving 3.40 g (0.02 mol) AgNO_3 in 40 mL $\text{NH}_3 \cdot \text{H}_2\text{O}$ solution. Under ultrasound irradiation, a specified amount of $\text{Ag}(\text{NH}_3)_2^+$ solution was added into a flask containing 0.25 g of $\text{Fe}_3\text{O}_4@\text{SiO}_2$ and 50 mL of DD-water. After sonicating for 30 min, a specified amount of KBr aqueous solution (0.5 M, the mole ratio of Ag to Br is 1:1) was injected and the mixture was sequentially stirred for 4 h at room temperature. Then, the precipitate was washed with DD-water, dried at 80 °C, and calcined at 500 °C for 3 h (Fe_3O_4 would convert into $\gamma\text{-Fe}_2\text{O}_3$). Finally, the obtained sample dispersed in DD-water was irradiated by UV light for 3 h, and dried at 80 °C for 6 h. Three representative $\text{Fe}_3\text{O}_4@\text{SiO}_2@\text{AgBr}$ samples with AgBr percentages of 24 wt.%, 42 wt.%, and 60 wt.% were denoted as $\text{Fe}_3\text{O}_4@\text{SiO}_2@\text{AgBr-1}$, $\text{Fe}_3\text{O}_4@\text{SiO}_2@\text{AgBr-2}$, and $\text{Fe}_3\text{O}_4@\text{SiO}_2@\text{AgBr-3}$, respectively. Similarly, their counterparts after calcination and light reduction were labeled as $\gamma\text{-Fe}_2\text{O}_3@\text{SiO}_2@\text{AgBr:Ag-1}$, $\gamma\text{-Fe}_2\text{O}_3@\text{SiO}_2@\text{AgBr:Ag-2}$, and $\gamma\text{-Fe}_2\text{O}_3@\text{SiO}_2@\text{AgBr:Ag-3}$, respectively.

For comparison, two control samples N-TiO_2 and $\text{Fe}_3\text{O}_4@\text{SiO}_2@\text{AgBr-C}$ were also synthesized according to the previous reports [7,24].

2.3. Characterization

X-ray diffraction (XRD) measurements were carried out with a Rigaku D/max 2550 VB/PC X-ray diffractometer using $\text{Cu K}\alpha$ radiation ($\lambda = 0.154056 \text{ nm}$) and a graphite monochromator. The morphologies of the samples were observed with scanning electron microscopy (SEM, JEOL JSM-6360 LV) and transmission electron microscopy (TEM, JEOL JEM2000EX). X-ray photoelectron spectroscopy (XPS) analysis was carried out on a Perkin–Elmer PHI 5000 Versaprobe system. The shift of the binding energies due to relative surface charging was corrected by assuming the position of adventitious C 1s line at 284.8 eV. UV-vis diffuse reflectance spectra (DRS) were measured with a SHIMADZU UV-2450 spectroscopy equipped with an integrating sphere assembly, using BaSO_4 as the reference material. Magnetic property measurements were performed on a Lakeshore 7407 vibrating sample magnetometer (VSM) at room temperature.

2.4. Photocatalytic degradation of acid orange 7

Azo dye acid orange 7 (AO7) was selected as a representative organic pollutant to evaluate the photocatalytic activity of the obtained core–shell structured photocatalyst. Photodegradation reactions were carried out with a home-made set-up, in which a 500 W halogen lamp equipped with a UV cutoff filter ($\lambda \geq 420 \text{ nm}$)

was used as light source. To maintain a constant temperature during the photocatalytic reaction, the lamp was cooled with flowing water in a quartz cylindrical jacket. For each test, 0.05 g of photocatalyst sample was added into a quartz tube containing 100 mL of AO7 aqueous solution (10 mg L^{-1}). Prior to light irradiation, the suspension was stirred for 30 min in the dark to attain the adsorption–desorption equilibrium for AO7 and dissolved oxygen on the surface of photocatalyst. At a given time interval, about 4 mL of suspension was withdrawn, magnetically separated, and filtered to remove the remained particles. The absorbance of AO7 solution was measured with a UV–vis spectrophotometer at 484 nm, which is the maximum absorption wavelength of AO7.

3. Results and discussion

3.1. Morphology and microstructures

Scheme 1 schematically illustrates the synthetic route of core–shell structured $\gamma\text{-Fe}_2\text{O}_3@\text{SiO}_2@\text{AgBr:Ag}$ composite. Firstly, near monodispersed Fe_3O_4 submicrospheres are synthesized via a solvothermal reaction in the presence of NaAc and PEG-20000. Here, NaAc not only prevents particle agglomeration as an electrostatic stabilization agent but also promotes the hydrolysis and reduction of FeCl_3 by increasing the alkalinity of reaction system [27], whereas, PEG acts as reduction agent to partly reduce Fe(OH)_3 into Fe(OH)_2 . Fe_3O_4 nanoparticles are produced through dehydration reaction and further aggregate to submicrospheres. Secondly, SiO_2 interlayer is coated on the surface of Fe_3O_4 core by Stöber method under ultrasound irradiation. Subsequently, AgBr shell layer is formed by electrostatic assembly. More specifically, after $\text{Ag}(\text{NH}_3)_2^+$ being added, the pH of $\text{Fe}_3\text{O}_4@\text{SiO}_2$ aqueous solution is much higher than the isoelectric point of SiO_2 synthesized by Stöber method ($\text{pH}=2\text{--}3$) [28–30]. In this case, the surface of $\text{Fe}_3\text{O}_4@\text{SiO}_2$ core–shell microspheres is negatively charged, which favors the adsorption of $\text{Ag}(\text{NH}_3)_2^+$ cations. When KBr is added, $\text{Ag}(\text{NH}_3)_2^+$ cations will react in situ with Br^- ions to form AgBr shell layer on $\text{Fe}_3\text{O}_4@\text{SiO}_2$ surface. Nextly, calcination at 500°C is conducted to make AgBr melt and closely contact with SiO_2 interlayer. In this process, Fe_3O_4 can convert to $\gamma\text{-Fe}_2\text{O}_3$. Finally, Ag nanoparticles are in situ produced on AgBr shell by UV light reduction. It should be mentioned that the SiO_2 interlayer between Fe_3O_4 ($\gamma\text{-Fe}_2\text{O}_3$) and AgBr can restrain the photocatalyst poisoning as well as the digestion of iron ions in the process of photocatalytic reaction.

Fig. 1 shows the XRD patterns of as-prepared Fe_3O_4 , calcined Fe_3O_4 , as-prepared $\text{Fe}_3\text{O}_4@\text{SiO}_2@\text{AgBr:Ag}-2$, calcined $\text{Fe}_3\text{O}_4@\text{SiO}_2@\text{AgBr:Ag}-2$, and calcined $\text{Fe}_3\text{O}_4@\text{SiO}_2@\text{AgBr:Ag}-2$. As shown in **Fig. 1A-a** and A-c, both as-prepared Fe_3O_4 and $\text{Fe}_3\text{O}_4@\text{SiO}_2@\text{AgBr:Ag}-2$ give diffraction peaks at $2\theta=30.10^\circ$, 35.42° , 43.05° , 53.39° , 56.94° , and 62.52° , corresponding to magnetite

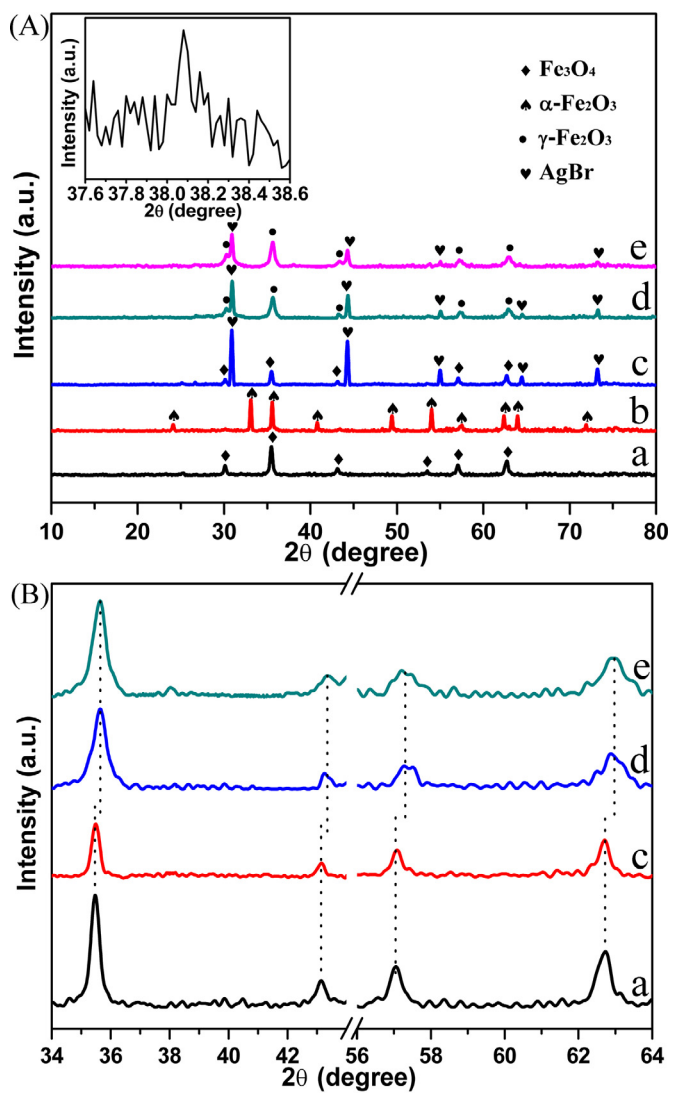


Fig. 1. (A) XRD patterns of (a) as-prepared Fe_3O_4 (without calcination), (b) calcined Fe_3O_4 ($\alpha\text{-Fe}_2\text{O}_3$), (c) as-prepared $\text{Fe}_3\text{O}_4@\text{SiO}_2@\text{AgBr:Ag}-2$, (d) calcined $\text{Fe}_3\text{O}_4@\text{SiO}_2@\text{AgBr:Ag}-2$ ($\gamma\text{-Fe}_2\text{O}_3@\text{SiO}_2@\text{AgBr:Ag}-2$), (e) calcined $\text{Fe}_3\text{O}_4@\text{SiO}_2@\text{AgBr:Ag}-2$ ($\gamma\text{-Fe}_2\text{O}_3@\text{SiO}_2@\text{AgBr:Ag}-2$). The inset is an enlarged XRD pattern of $\gamma\text{-Fe}_2\text{O}_3@\text{SiO}_2@\text{AgBr:Ag}-2$ in the range of $37.6\text{--}38.6^\circ$. (B) Enlarged XRD patterns of as-prepared Fe_3O_4 , as-prepared $\text{Fe}_3\text{O}_4@\text{SiO}_2@\text{AgBr:Ag}-2$, and calcined $\text{Fe}_3\text{O}_4@\text{SiO}_2@\text{AgBr:Ag}-2$ ($\gamma\text{-Fe}_2\text{O}_3@\text{SiO}_2@\text{AgBr:Ag}-2$) in the range of $34\text{--}44^\circ$ and $56\text{--}64^\circ$.

Fe_3O_4 (220), (311), (400), (422), (511), and (440) plane reflections, respectively (JCPDS 19-629). Comparatively, the calcined Fe_3O_4 presents diffraction peaks at $2\theta=24.14^\circ$, 33.15° , 35.61° , 40.85° , 49.48° , 54.09° , 62.45° , and 63.99° , which should be indexed to hematite $\alpha\text{-Fe}_2\text{O}_3$ (JCPDS 33-664). In the case of calcined $\text{Fe}_3\text{O}_4@\text{SiO}_2@\text{AgBr:Ag}-2$ and $\text{Fe}_3\text{O}_4@\text{SiO}_2@\text{AgBr:Ag}-2$, the diffraction peaks emerge at $2\theta=30.24^\circ$, 35.63° , 43.28° , 53.73° , 57.27° , and 62.93° , which should be attributed to magnetite Fe_2O_3 ($\gamma\text{-Fe}_2\text{O}_3$) (220), (311), (400), (422), (511), and (440) plane reflections, respectively (JCPDS 39-1346). As shown in **Fig. 1B**, the diffraction peaks of $\gamma\text{-Fe}_2\text{O}_3$ shift slightly to the higher angles compared with those of Fe_3O_4 (**Fig. 1B**). Although the diffraction peaks of Fe_3O_4 and $\gamma\text{-Fe}_2\text{O}_3$ are very similar, they are ascribed to different space groups ($Fd\bar{3}m$ and $P4_132$ for Fe_3O_4 and $\gamma\text{-Fe}_2\text{O}_3$, respectively), and have different lattice parameters (8.396\AA and 8.351\AA for Fe_3O_4 and $\gamma\text{-Fe}_2\text{O}_3$) [31]. It is worth noting that $\alpha\text{-Fe}_2\text{O}_3$ and $\gamma\text{-Fe}_2\text{O}_3$ are, respectively, obtained by calcining bare Fe_3O_4 and $\text{Fe}_3\text{O}_4@\text{SiO}_2@\text{AgBr}$. Similar results have also been reported by



Scheme 1. Schematic diagram illustrating the synthetic route of core–shell structured $\gamma\text{-Fe}_2\text{O}_3@\text{SiO}_2@\text{AgBr:Ag}$ composite.

the previous studies [32–35]. During calcination process, bare Fe_3O_4 not only contacts with oxygen more thoroughly but also experiences more thermal radiation when compared with Fe_3O_4 enclosed by SiO_2 and AgBr , favorable to the formation of more thermodynamically stable $\alpha\text{-Fe}_2\text{O}_3$ rather than metastable $\gamma\text{-Fe}_2\text{O}_3$. As-prepared $\text{Fe}_3\text{O}_4@\text{SiO}_2@\text{AgBr-2}$, $\gamma\text{-Fe}_2\text{O}_3@\text{SiO}_2@\text{AgBr-2}$, and $\gamma\text{-Fe}_2\text{O}_3@\text{SiO}_2@\text{AgBr-3}$ give very approximate diffraction peaks at $2\theta=30.96^\circ$, 44.35° , 55.04° and 73.26° , indexed to AgBr (2 0 0), (2 2 0), (2 2 2) and (4 2 0) plane reflections, respectively (JCPDS: 06-0438). As shown in Fig. 1A-c and A-d, the diffraction peaks assigned to AgBr becomes weaker after calcination, probably due to the melt of AgBr particles. The average particle size of AgBr in $\gamma\text{-Fe}_2\text{O}_3@\text{SiO}_2@\text{AgBr}$ was calculated to be 36.2 nm, according to Debye–Scherrer formula [36]. For $\gamma\text{-Fe}_2\text{O}_3@\text{SiO}_2@\text{AgBr:Ag-2}$, the Y-axis enlarged inset shows a weak peak around the scattering angle of $2\theta=38.12^\circ$, corresponding to the cubic phase of Ag (1 1 1) (JCPDS 04-0783), which implies that metallic Ag^0 has produced after UV light irradiation. For all samples, no peak assigned to Si can be detected because of its amorphous characteristics.

Fig. 2A shows the SEM image of as-prepared Fe_3O_4 magnetic cores, which indicates that Fe_3O_4 cores exhibit regular spherical shape with a diameter of about 250 nm. By close observation, it can be clearly seen that each of these microspheres consists of many small primary particles with a size of ~ 30 nm (Fig. 2B).

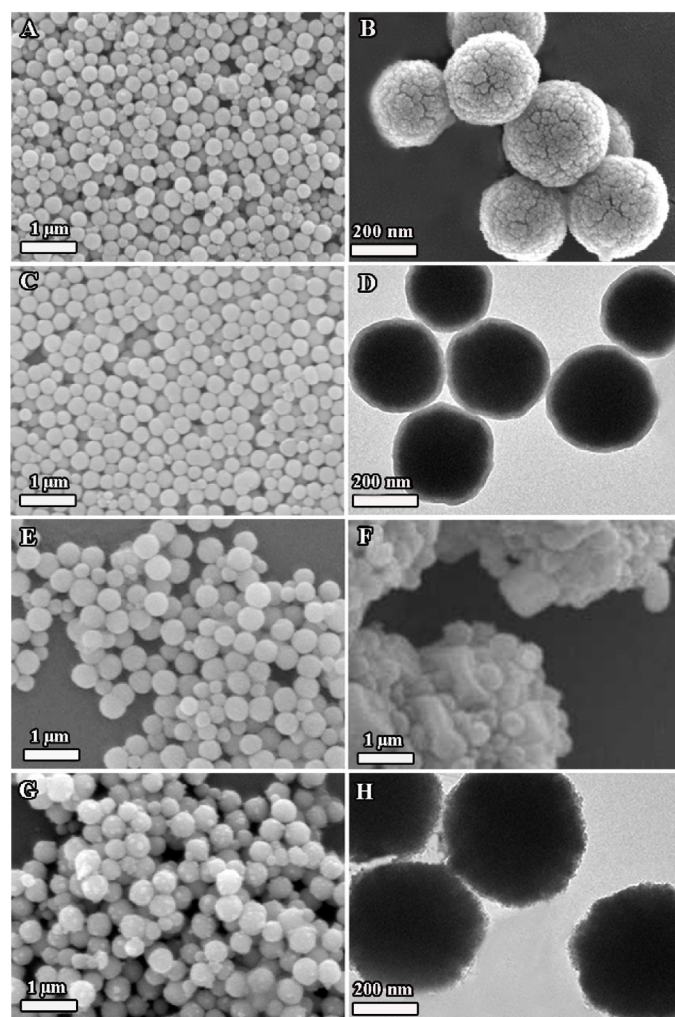


Fig. 2. (A) SEM and (B) TEM images of as-prepared Fe_3O_4 . (C) SEM and (D) TEM images of as-prepared $\text{Fe}_3\text{O}_4@\text{SiO}_2$. (E) SEM image of $\text{Fe}_3\text{O}_4@\text{SiO}_2@\text{AgBr-2}$. (F) SEM image of $\text{Fe}_3\text{O}_4@\text{SiO}_2@\text{AgBr-3}$. (G) SEM image of $\gamma\text{-Fe}_2\text{O}_3@\text{SiO}_2@\text{AgBr-2}$. (H) TEM image of $\gamma\text{-Fe}_2\text{O}_3@\text{SiO}_2@\text{AgBr-2}$.

The growth of Fe_3O_4 magnetite cores probably follows a two-stage growth model: firstly, primary nanocrystals nucleate in a supersaturated solution. Subsequently, they aggregate into sub-microspheres to minimize the total surface energy. This structure makes Fe_3O_4 magnetic cores show much higher saturation magnetization than individual nanoparticle. As a result, these magnetic cores can be rapidly separated by an external magnetic field [20,37]. From Fig. 2C and D, it can be seen that SiO_2 interlayer with a thickness of ~ 15 nm is homogenously coated on the surface of Fe_3O_4 core. When the loading amount of AgBr is 42 wt.%, well-dispersed $\text{Fe}_3\text{O}_4@\text{SiO}_2@\text{AgBr}$ microspheres are presented, along with the increase of diameter from ~ 280 nm to ~ 350 nm (Fig. 2E). By contrast, $\text{Fe}_3\text{O}_4@\text{SiO}_2@\text{AgBr}$ microspheres begin to aggregate together when the amount of AgBr reaches 60 wt.% (Fig. 2F). After heat treatment and light reduction, $\gamma\text{-Fe}_2\text{O}_3@\text{SiO}_2@\text{AgBr:Ag}$ still remains well-dispersed spherical morphology (Fig. 2G), similar to its precursor $\text{Fe}_2\text{O}_3@\text{SiO}_2@\text{AgBr}$. Compared with $\text{Fe}_3\text{O}_4@\text{SiO}_2$ (D), the surface of $\gamma\text{-Fe}_2\text{O}_3@\text{SiO}_2@\text{AgBr:Ag}$ becomes very rough, probably due to the formation of AgBr shell and Ag nanoparticles.

The elemental composition and surface chemical status of the samples were analyzed by X-ray photoelectron spectroscopy (XPS). Fig. 3A shows the Fe 2p XPS spectra of as-prepared Fe_3O_4 and calcined Fe_3O_4 ($\alpha\text{-Fe}_2\text{O}_3$). Compared with Fe 2p_{1/2} peak, Fe 2p_{3/2} peak seems stronger and has bigger area, which is due to spin-orbit ($j-j$) coupling [38]. For as-prepared Fe_3O_4 (Fig. 3A-a), there are two peaks located at 711.0 eV and 724.6 eV, attributed to Fe 2p_{3/2} and Fe 2p_{1/2}, respectively [39,40]. By contrast, calcined Fe_3O_4 ($\alpha\text{-Fe}_2\text{O}_3$) not only gives two peaks at 710.7 eV (Fe 2p_{3/2}) and 724.2 eV (Fe 2p_{1/2}) but also presents a peak at 719.0 eV (Fig. 3A-b), which is the characteristic satellite peak of Fe^{3+} in Fe_2O_3 [39–41]. The survey spectrum of $\text{Fe}_3\text{O}_4@\text{SiO}_2$ (Fig. 3B) clearly shows the characteristic peaks of Si , O , and C , in which C1s peak is from adventitious carbon. After coating SiO_2 interlayer, the peaks attributed to Fe 2p almost cannot be detected, indicating that Fe_3O_4 has been tightly wrapped by SiO_2 shell. Fig. 3C shows the Ag 3d and Br 2p XPS spectra of $\gamma\text{-Fe}_2\text{O}_3@\text{SiO}_2@\text{AgBr:Ag-2}$. The deconvoluted Ag 3d peaks indicate that two components coexist in Ag 3d_{5/2} and 3d_{3/2} signals. According to the previous reports [42,43], one set of peaks located at 367.6 eV and 373.6 eV should be attributed to Ag^+ in AgBr , while the other set at 368.3 eV and 374.3 eV should be assigned to metallic silver (Ag^0). The double peaks located at 68.1 eV and 69.1 eV can be assigned to the characteristic doublets of Br 2p_{3/2} and Br 2p_{1/2} [44,45].

3.2. Optical and magnetic performances

Fig. 4 shows the UV-vis DRS spectra of the prepared samples. $\text{Fe}_3\text{O}_4@\text{SiO}_2$ and $\text{Fe}_3\text{O}_4@\text{SiO}_2@\text{AgBr-2}$ exhibit slightly weaker absorption in the range of 550–750 nm than as-prepared Fe_3O_4 , probably resulting from the light reflection and refraction of SiO_2 and AgBr shells. Beneficial from Ag SPR [17,19,42], $\text{Fe}_3\text{O}_4@\text{SiO}_2@\text{AgBr:Ag-2}$ shows an enhanced absorption in the visible light region compared with $\text{Fe}_3\text{O}_4@\text{SiO}_2@\text{AgBr}$. It is well known that the SPR absorption band of noble metal nanoparticles depends on their particle size [46]. $\gamma\text{-Fe}_2\text{O}_3@\text{SiO}_2@\text{AgBr-2}$ can harvest the light of the whole visible region, implying that Ag nanoparticles loaded on AgBr surface show broad size distribution.

Fig. 5 shows the magnetic hysteresis curves of $\text{Fe}_3\text{O}_4@\text{SiO}_2$, $\gamma\text{-Fe}_2\text{O}_3@\text{SiO}_2$, $\gamma\text{-Fe}_2\text{O}_3@\text{SiO}_2@\text{AgBr:Ag-2}$, and $\text{Fe}_3\text{O}_4@\text{SiO}_2@\text{AgBr-C}$. The saturation magnetization (M_s) values for $\text{Fe}_3\text{O}_4@\text{SiO}_2$ and $\gamma\text{-Fe}_2\text{O}_3@\text{SiO}_2$ were estimated to be 60 emu/g and 57 emu/g, respectively. Since the content of Fe_3O_4 in $\text{Fe}_3\text{O}_4@\text{SiO}_2$ (78.0 wt.%) is similar to that of $\gamma\text{-Fe}_2\text{O}_3$ in $\gamma\text{-Fe}_2\text{O}_3@\text{SiO}_2$ (78.0 wt.%), it means that the structure change from Fe_3O_4 to $\gamma\text{-Fe}_2\text{O}_3$ almost has no influence on saturation magnetization. The saturation magnetization (M_s), remanent magnetization (M_r),

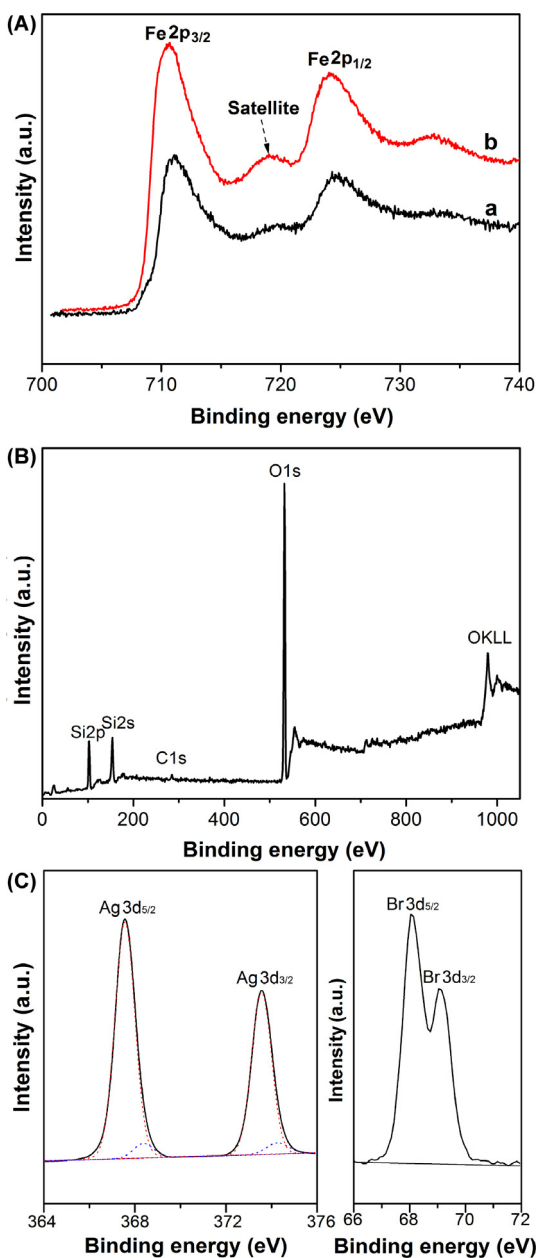


Fig. 3. (A) Fe 2p XPS spectra of (a) as-prepared Fe_3O_4 and calcined Fe_3O_4 (α - Fe_2O_3). (B) XPS survey spectrum of $\text{Fe}_3\text{O}_4@\text{SiO}_2$. (C) Ag 3d and Br 3d XPS spectra of γ - $\text{Fe}_2\text{O}_3@\text{SiO}_2@\text{AgBr:Ag-2}$.

and coercivity (H_c) of γ - $\text{Fe}_2\text{O}_3@\text{SiO}_2@\text{AgBr:Ag-2}$ were evaluated to be 32.8 emu/g, 0.87 emu/g, and 23.2 G, respectively, suggesting that γ - $\text{Fe}_2\text{O}_3@\text{SiO}_2@\text{AgBr:Ag-2}$ exhibits superparamagnetic behavior to some extent. According to the γ - Fe_2O_3 content in γ - $\text{Fe}_2\text{O}_3@\text{SiO}_2@\text{AgBr:Ag}$ (45.6%), the M_s value of γ - $\text{Fe}_2\text{O}_3@\text{SiO}_2@\text{AgBr:Ag}$ can be normalized to 71.8 emu/g for γ - Fe_2O_3 , which is only slightly smaller than the theoretical M_s value of bulk γ - Fe_2O_3 at room temperature (76 emu/g) [47,48]. The M_s value of γ - $\text{Fe}_2\text{O}_3@\text{SiO}_2@\text{AgBr:Ag}$ is much larger than that of $\text{Fe}_3\text{O}_4@\text{SiO}_2@\text{AgBr-C}$, implying that the former can be more easily separated than the latter by an external magnetic field.

3.3. Photocatalytic activity and magnetic recycling

Photocatalytic degradation of AO7 was selected as a probe reaction to evaluate the photocatalytic activity of the different

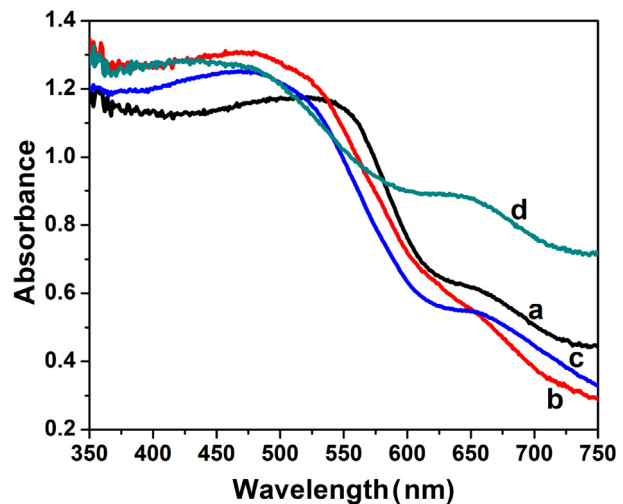


Fig. 4. UV-vis DRS spectra of (a) as-prepared Fe_3O_4 , (b) $\text{Fe}_3\text{O}_4@\text{SiO}_2$, (c) $\text{Fe}_3\text{O}_4@\text{SiO}_2@\text{AgBr-2}$, and (d) γ - $\text{Fe}_2\text{O}_3@\text{SiO}_2@\text{AgBr:Ag-2}$.

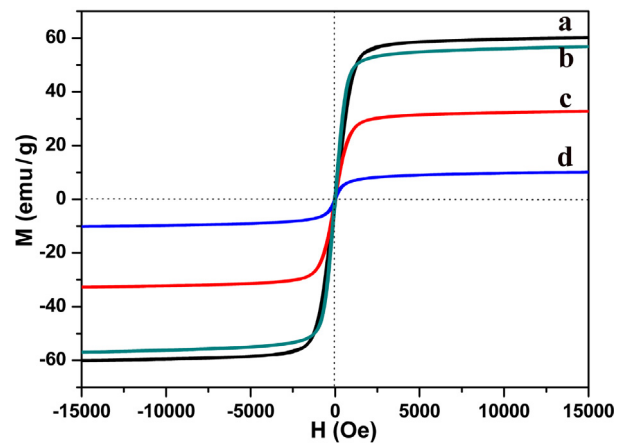


Fig. 5. Magnetic hysteresis curves of (a) $\text{Fe}_3\text{O}_4@\text{SiO}_2$, (b) γ - $\text{Fe}_2\text{O}_3@\text{SiO}_2$, (c) γ - $\text{Fe}_2\text{O}_3@\text{SiO}_2@\text{AgBr:Ag-2}$, and (d) $\text{Fe}_3\text{O}_4@\text{SiO}_2@\text{AgBr-C}$ at room temperature.

samples. The degradation curves of AO7 over the different samples as a function of visible light irradiation time are plotted in Fig. 6A, in which C_0 is the concentration of AO7 after adsorption-desorption equilibrium, whereas C represents the corresponding concentration at a certain time. As shown in Fig. 6A, in the absence of AgBr, $\text{Fe}_3\text{O}_4@\text{SiO}_2$ is inert for AO7 degradation under visible light irradiation. Compared with N-TiO₂ and $\text{Fe}_3\text{O}_4@\text{SiO}_2@\text{AgBr-C}$, γ - $\text{Fe}_2\text{O}_3@\text{SiO}_2@\text{AgBr:Ag-2}$ shows much higher photocatalytic activity for AO7 degradation. After visible light irradiation for 20 min, the degradation rates of AO7 over N-TiO₂, $\text{Fe}_3\text{O}_4@\text{SiO}_2@\text{AgBr-C}$, and γ - $\text{Fe}_2\text{O}_3@\text{SiO}_2@\text{AgBr:Ag-2}$ are 17.3%, 26.4%, and 93.1%, respectively. The influence of AgBr content on the photocatalytic activity was also investigated. As shown in Fig. 6B, the photocatalytic activity of γ - $\text{Fe}_2\text{O}_3@\text{SiO}_2@\text{AgBr:Ag}$ increases gradually with increasing AgBr content. However, it should be noted that the increase rate of photocatalytic activity is much lower than that of AgBr content. Moreover, too much AgBr coating can lead to the aggregation of $\text{Fe}_3\text{O}_4@\text{SiO}_2@\text{AgBr}$ microspheres (Fig. 2F), which is detrimental to the recovery of photocatalyst sample. Here, it seems that 42 wt.% is a suitable AgBr content for obtaining both high photocatalytic activity and separation efficiency.

Magnetic separation is a promising technique for catalyst recycling because it not only prevents the loss of catalyst but also

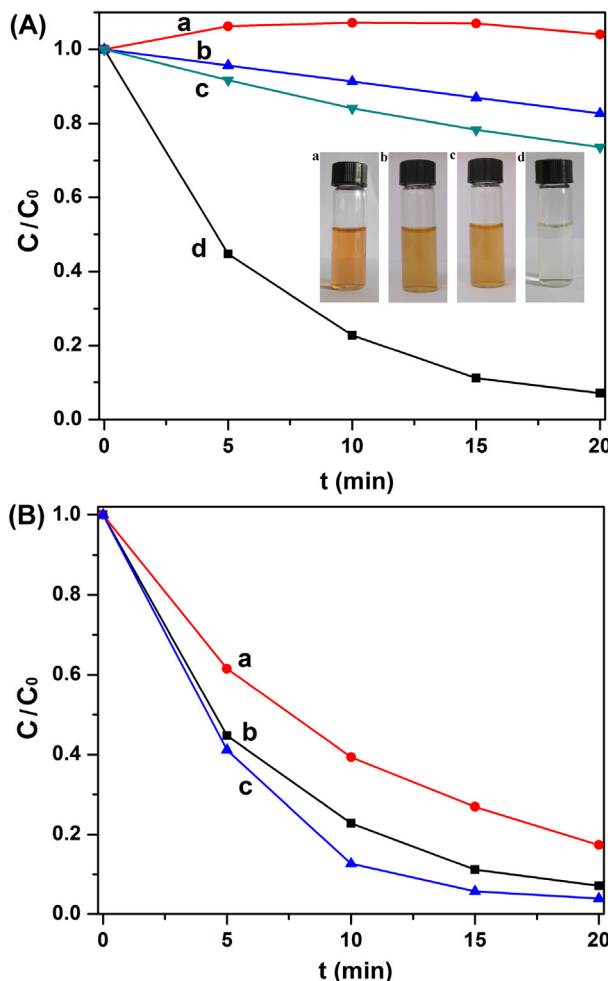


Fig. 6. (A) Degradation curves of AO7 under visible light over the different samples: (a) $\gamma\text{-Fe}_2\text{O}_3@\text{SiO}_2$; (b) N-TiO₂; (c) $\text{Fe}_3\text{O}_4@\text{SiO}_2@\text{AgBr-C}$; (d) $\gamma\text{-Fe}_2\text{O}_3@\text{SiO}_2@\text{AgBr:Ag}$. The inset is the photos of AO7 solutions after photocatalytic degradation for 20 min over the four samples. (B) Degradation curves of AO7 over $\gamma\text{-Fe}_2\text{O}_3@\text{SiO}_2@\text{AgBr:Ag}$ samples with different AgBr contents: (a) $\gamma\text{-Fe}_2\text{O}_3@\text{SiO}_2@\text{AgBr:Ag-1}$ ($W_{\text{AgBr}} = 24 \text{ wt.\%}$); (b) $\gamma\text{-Fe}_2\text{O}_3@\text{SiO}_2@\text{AgBr:Ag-2}$ ($W_{\text{AgBr}} = 42 \text{ wt.\%}$); (c) $\gamma\text{-Fe}_2\text{O}_3@\text{SiO}_2@\text{AgBr:Ag-3}$ ($W_{\text{AgBr}} = 60 \text{ wt.\%}$).

saves time. To verify the magnetic separation property of core-shell structured $\gamma\text{-Fe}_2\text{O}_3@\text{SiO}_2@\text{AgBr:Ag}$ composite, a cubic Nd-Fe-B magnet (50 mm × 50 mm × 10 mm) was employed to conduct the magnetic separation test. As shown in Fig. 7A, the representative

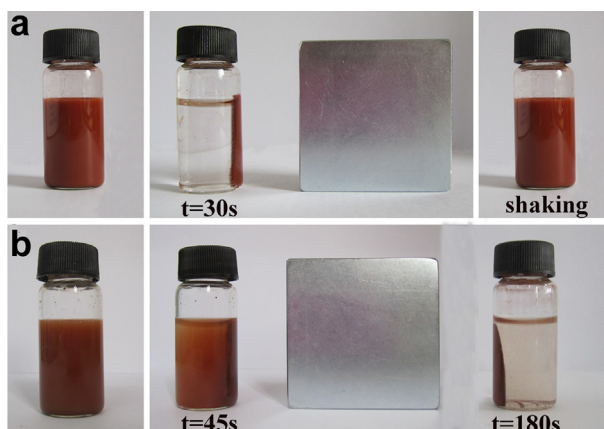


Fig. 7. Magnetic separation tests for (a) $\gamma\text{-Fe}_2\text{O}_3@\text{SiO}_2@\text{AgBr:Ag-2}$ and (b) $\text{Fe}_3\text{O}_4@\text{SiO}_2@\text{AgBr-C}$ using a cubic Nd-Fe-B magnet (50 mm × 50 mm × 10 mm).

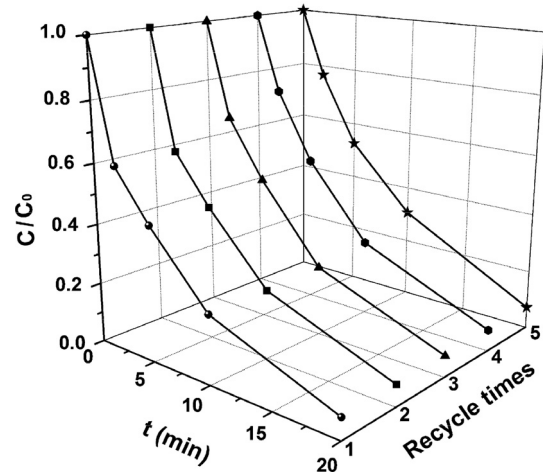
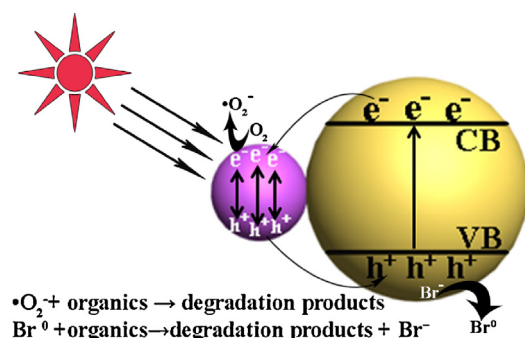


Fig. 8. Cycling runs in the photocatalytic degradation of AO7 over $\gamma\text{-Fe}_2\text{O}_3@\text{SiO}_2@\text{AgBr:Ag-2}$ photocatalyst.

sample $\gamma\text{-Fe}_2\text{O}_3@\text{SiO}_2@\text{AgBr:Ag-2}$ can be totally collected within 30 s. Once the external magnetic field was removed, only a slight shaking can make the magnetic particles recover to their original dispersed state. Benefiting from the high M_e value as well as narrow size distribution, all composite microspheres rapidly migrate under the external magnetic field, resulting in a high separation efficiency. In contrast, only part $\text{Fe}_3\text{O}_4@\text{SiO}_2@\text{AgBr-C}$ was collected after the magnetic field irradiation for 45 s, and another 180 s is necessary for completely separating the particles. The control sample shows wide size distribution, in which the smaller particles migrate slower than the bigger ones, resulting in a longer magnetic separation time.

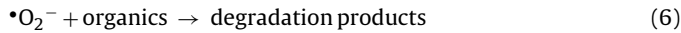
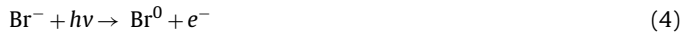
Besides photocatalytic activity, the stability is also very important to a photocatalyst for its practical application. To test the stability of $\gamma\text{-Fe}_2\text{O}_3@\text{SiO}_2@\text{AgBr:Ag}$ composite photocatalyst, cycling experiments were carried out using $\gamma\text{-Fe}_2\text{O}_3@\text{SiO}_2@\text{AgBr:Ag-2}$ as a representative sample. As shown in Fig. 8, the photocatalytic efficiency has no obvious decrease after five cycles of degrading AO7, proving that the fabricated core-shell structured composite $\gamma\text{-Fe}_2\text{O}_3@\text{SiO}_2@\text{AgBr:Ag}$ is a stable photocatalyst under visible light irradiation.

AgBr can absorb the light below 480 nm, while Ag NPs can absorb the light higher than 450 nm by SPR effect [17,19,49]. The cooperation of Ag NPs and AgBr makes AgBr@Ag shell layer can respond to the light in the whole visible region. Consequently, $\gamma\text{-Fe}_2\text{O}_3@\text{SiO}_2@\text{AgBr:Ag}$ showed much higher visible photocatalytic activity than N-TiO₂. The degradation mechanism of organic pollutants over $\gamma\text{-Fe}_2\text{O}_3@\text{SiO}_2@\text{AgBr:Ag}$ plasmonic photocatalyst is schematically illustrated in Scheme 2. When AgBr@Ag shell is irradiated by visible light, Ag NPs produce photogenerated electrons



Scheme 2. Proposed degradation mechanism of organic pollutants over $\gamma\text{-Fe}_2\text{O}_3@\text{SiO}_2@\text{AgBr:Ag}$ photocatalyst.

and holes, which can be separated by the SPR-induced local electromagnetic field (Eq. (1)) [17]. The surface of AgBr grains is terminated by Br⁻ ions and is therefore negatively charged. Due to the polarization effect of negatively charged AgBr surface, the electrons are transferred to the surface of Ag NP farthest away from the Ag@AgBr interface, while holes are transferred to the surface of AgBr [17]. Subsequently, the electrons will be trapped by adsorbed O₂ to form •O₂⁻ (Eq. (2)), while the holes will combine with Br⁻ ions to form Br⁰ atoms (radicals) (Eq. (3)). In addition, AgBr also can product electrons and Br⁰ atoms under visible light irradiation (Eq. (4)). Both Br⁰ and •O₂⁻ are active species responsible for the degradation of organic pollutants (Eqs. (5) and (6)).



4. Conclusions

In summary, we fabricated core-shell structured γ-Fe₂O₃@SiO₂@AgBr:Ag microspheres with narrow size distribution by a versatile multistep route, including solvothermal method to synthesize magnetic core, modified Stöber method to coat SiO₂ interlayer, electrostatic assembly to deposit AgBr shell, and light reduction to form Ag nanoparticles. Especially, electrostatic assembly was found to be a competent method for forming AgBr shell. The spherical core with a diameter of 250 nm consists of many primary magnetic nanoparticles, making the composite photocatalyst show high saturation magnetization under the premise of keeping a certain superparamagnetic property. SiO₂ interlayer plays a key role in enhancing the chemical stability of magnetic core as well as preventing the deterioration of photocatalytic activity. AgBr can response to part visible light, at the same time Ag nanoparticles can harvest visible light by surface plasmon resonance. The cooperation of Ag nanoparticles and AgBr makes γ-Fe₂O₃@SiO₂@AgBr:Ag can effectively harvest visible light. As a result, composite photocatalyst γ-Fe₂O₃@SiO₂@AgBr:Ag exhibited excellent visible light photocatalytic activity for A07 degradation. Beneficial from the narrow size distribution as well as high saturation magnetization and superparamagnetic property, the core-shell structured photocatalyst γ-Fe₂O₃@SiO₂@AgBr:Ag shows excellent magnetic separation and recovery performances. The optimal loading amount of AgBr for obtaining both uniform morphology and high activity is ~42 wt%. Due to its excellent visible light activity for organic contaminant degradation as well as effective magnetic separation efficiency, the core-shell structured composite photocatalyst can be potentially applied in waste water treatment and other photocatalysis fields. Moreover, as a universal synthetic route, the technique reported here can be used to fabricate other magnetically separable photocatalysts.

Acknowledgements

This work has been supported by the National Natural Science Foundation of China (21277046, 21047002, 21173077), the Shanghai Committee of Science and Technology (13NM1401000), the Shanghai Natural Science Foundation (10ZR1407400), the

National Basic Research Program of China (973 Program, 2010CB732306), and the Project of International Cooperation of the Ministry of Science and Technology of China (2011DFA50530).

References

- [1] M.N. Chong, B. Jin, C.W.K. Chow, C. Saint, *Water Res.* 44 (2010) 2997–3027.
- [2] X. Chen, S. Shen, L. Guo, S.S. Mao, *Chem. Rev.* 110 (2010) 6503–6570.
- [3] Y.J. Zang, R. Farnood, *Appl. Catal. B: Environ.* 79 (2008) 334–340.
- [4] B.Z. Tian, C.Z. Li, J.L. Zhang, *Chem. Eng. J.* 191 (2012) 402–409.
- [5] B.Z. Tian, C.Z. Li, F. Gu, H.B. Jiang, Y.J. Hu, J.L. Zhang, *Chem. Eng. J.* 151 (2009) 220–227.
- [6] R. Asahi, T. Morikawa, T. Ohwaki, K. Aoki, Y. Taga, *Science* 293 (2001) 269–271.
- [7] M.Y. Xing, Y.M. Wu, J.L. Zhang, F. Chen, *Nanoscale* 2 (2010) 1233–1239.
- [8] E. Bae, W. Choi, J. Park, H.S. Shin, S.B. Kim, J.S. Lee, *J. Phys. Chem. B* 108 (2004) 14093–14101.
- [9] W.W. Zou, J.L. Zhang, F. Chen, *Mater. Lett.* 64 (2010) 1710–1712.
- [10] H. Zhang, Y.F. Zhu, *J. Phys. Chem. C* 114 (2010) 5822–5826.
- [11] C. Zhang, Y.F. Zhu, *Chem. Mater.* 17 (2005) 3537–3545.
- [12] Z.G. Zou, J.H. Ye, H. Arakawa, *Nature* 414 (2001) 625–627.
- [13] M. Anpo, M. Takeuchi, *J. Catal.* 216 (2003) 505–516.
- [14] B.Z. Tian, J.L. Zhang, T.Z. Tong, F. Chen, *Appl. Catal. B* 79 (2008) 394–401.
- [15] H. Liang, H. Yang, W. Wang, J. Li, H. Xu, *J. Am. Chem. Soc.* 131 (2009) 6068–6069.
- [16] K. Awazu, M. Fujimaki, C. Rockstuhl, J. Tominaga, H. Murakami, Y. Ohki, N. Yoshida, T. Watanabe, *J. Am. Chem. Soc.* 130 (2008) 1676–1680.
- [17] P. Wang, B.B. Huang, X.Y. Qin, X.Y. Zhang, Y. Dai, J.Y. Wei, M.H. Whangbo, *Angew. Chem. Int. Ed.* 47 (2008) 7931–7933.
- [18] P. Wang, B.B. Huang, Y. Dai, M.H. Whangbo, *Phys. Chem. Chem. Phys.* 14 (2012) 9813–9825.
- [19] B.Z. Tian, J.L. Zhang, *Catal. Surv. Asia* 16 (2012) 210–230.
- [20] M.M. Ye, Q. Zhang, Y.X. Hu, J.P. Ge, Z.D. Lu, L. He, Z.L. Chen, Y.D. Yin, *Chem. Eur. J.* 16 (2010) 6243–6250.
- [21] X. Guo, N. Chen, C.P. Feng, Y.N. Yang, B.G. Zhang, G. Wang, Z.Y. Zhang, *Catal. Commun.* 38 (2013) 26–30.
- [22] Y.X. Zhang, X.Y. Yu, Y. Jia, Z. Jin, J.H. Liu, X.J. Huang, *Eur. J. Inorg. Chem.* 33 (2011) 5096–5104.
- [23] X. Xu, X.P. Shen, G.X. Zhu, L.Q. Jing, X.S. Liu, K.M. Chen, *Chem. Eng. J.* 200–202 (2012) 521–531.
- [24] G.T. Li, K.H. Wong, X.W. Zhang, C. Hu, J.C. Yu, R.C.Y. Chan, P.K. Wong, *Chemosphere* 76 (2009) 1185–1191.
- [25] C.H. An, X.J. Ming, J.Z. Wang, S.T. Wang, *J. Mater. Chem.* 22 (2012) 5171–5176.
- [26] J.F. Guo, B.W. Ma, A.Y. Yin, K.N. Fan, W.L. Dai, *Appl. Catal. B: Environ.* 101 (2011) 580–586.
- [27] B. Luo, X.J. Song, F. Zhang, A. Xia, W.L. Yang, J.H. Hu, C.C. Wang, *Langmuir* 26 (3) (2010) 1674–1679.
- [28] S. Shibata, T. Taniguchi, T. Yano, M. Yamane, *J. Sol-Gel Sci. Technol.* 10 (1997) 263–268.
- [29] D.H. Ryu, S.C. Kim, S.M. Koo, D.P. Kim, *J. Sol-Gel Sci. Technol.* 26 (2003) 489–493.
- [30] X.A. Fu, S. Qutubuddin, *Colloid Surf. A* 178 (2001) 151–156.
- [31] D. Li, W.Y. Teoh, C. Selomulya, R.C. Woodward, P. Munroe, R. Amal, *J. Mater. Chem.* 17 (2007) 4876–4884.
- [32] C.X. Wang, L.W. Yin, L.Y. Zhang, L. Kang, X.F. Wang, R. Gao, *J. Phys. Chem. C* 113 (2009) 4008–4011.
- [33] C.L. Wang, J.T. Yan, X.J. Cui, H.Y. Wang, *J. Colloid Interf. Sci.* 354 (2011) 94–99.
- [34] H. Deng, X.L. Li, Q. Peng, X. Wang, J.P. Chen, Y.D. Li, *Angew. Chem. Int. Ed.* 44 (2005) 2782–2785.
- [35] Y.T. Zhang, L.L. Li, W.F. Ma, Y. Zhang, M. Yu, J. Guo, H.J. Lu, C.C. Wang, *ACS Appl. Mater. Interfaces* 5 (2013) 614–621.
- [36] J. Lin, Y. Lin, P. Liu, M.J. Meziani, L.F. Allard, Y.P. Sun, *J. Am. Chem. Soc.* 124 (2002) 11514–11518.
- [37] E. Taboada, R. Solanas, E. Rodríguez, R. Weissleder, A. Roig, *Adv. Funct. Mater.* 19 (2009) 2319–2324.
- [38] T. Yamashita, P. Hayes, *Appl. Surf. Sci.* 254 (2008) 2441–2449.
- [39] C.J. Jia, L.D. Sun, F. Luo, X.D. Han, L.J. Heyderman, Z.G. Yan, C.H. Yan, K. Zheng, *J. Am. Chem. Soc.* 130 (2008) 16968–16977.
- [40] G.B. Sun, B.X. Dong, M.H. Cao, B.Q. Wei, C.W. Hu, *Chem. Mater.* 23 (2011) 1587–1593.
- [41] X.L. Hu, J.C. Yu, J.M. Gong, *J. Phys. Chem. C* 111 (2007) 11180–11185.
- [42] R.F. Dong, B.Z. Tian, C.Y. Zeng, T.Y. Li, T.T. Wang, J.L. Zhang, *J. Phys. Chem. C* 117 (2013) 213–220.
- [43] P. Wang, B.B. Huang, Z.Z. Lou, X.Y. Zhang, X.Y. Qin, Y. Dai, Z.K. Zheng, X.N. Wang, *Chem. Eur. J.* 16 (2010) 538–544.
- [44] P. Wang, B.B. Huang, X.Y. Qin, X.Y. Zhang, Y. Dai, M.H. Whangbo, *Inorg. Chem.* 48 (2009) 10697–10702.
- [45] R.F. Dong, B.Z. Tian, J.L. Zhang, T.T. Wang, Q.S. Tao, S.Y. Bao, F. Yang, C.Y. Zeng, *Catal. Commun.* 38 (2013) 16–20.
- [46] S. Linic, P. Christopher, D.B. Ingram, *Nat. Mater.* 10 (2011) 911–921.
- [47] B.D. Cullity, *Introduction to Magnetic Materials*, Addison-Wesley, Reading, MA, 1972, pp. 201 (pp. 383–441).
- [48] K. Mori, S. Kanai, T. Hara, T. Mizugaki, K. Ebitani, K. Jitsukawa, K. Kaneda, *Chem. Mater.* 19 (2007) 1249–1256.
- [49] M.S. Zhu, P.L. Chen, M.H. Liu, *Langmuir* 28 (2012) 3385–3390.